

## **Simulation of semi-solid material mechanical behavior using a combined discrete/finite element method**

M. Sistaninia<sup>1</sup>, A.B. Phillion<sup>1,2</sup>, J.-M. Drezet<sup>1</sup>, M. Rappaz<sup>1</sup>

1. Computational Materials Laboratory, Ecole Polytechnique Fédérale de Lausanne, Lausanne, Switzerland
2. School of Engineering, University of British Columbia Okanagan, Kelowna, Canada

### **Abstract:**

As a necessary step toward the quantitative prediction of hot tearing defects, a 3D stress-strain simulation based on a combined Finite Element (FE) / Discrete Element Method (DEM) has been developed that is capable of predicting the mechanical behavior of semi-solid metallic alloys during solidification. The solidification model used for generating the initial solid-liquid structure is based on a Voronoi tessellation of randomly distributed nucleation centers and a solute diffusion model for each element of this tessellation. At a given fraction of solid, deformation is then simulated with the solid grains being modeled using an elasto-viscoplastic constitutive law, while the remaining liquid layers at grain boundaries are approximated by flexible connectors, each consisting of a spring element and a damper element acting in parallel. The model predictions have been validated against Al-Cu alloy experimental data from the literature. The results show that a combined FE/DEM

approach is able to express the overall mechanical behavior of semi-solid alloys at the macro scale based on the morphology of the grain structure. For the first time, the localization of strain in the intergranular regions is taken into account. Thus, this approach constitutes an indispensable step towards the development of a comprehensive model of hot tearing.

Keywords: Microstructure; FE modelling; Semi-solid; Discrete element method; Mechanical behavior

## **1. Introduction:**

Hot tearing is a spontaneous failure of semi-solid metallic alloys that results in an intergranular fracture profile. This defect occurs during casting, near the end of solidification, especially in low solute content alloys. Hot tearing can be partially controlled by process changes such as mold design and/or cooling condition during solidification. However, a prerequisite to efficiently making such process changes is the development of a fundamental understanding of this defect's formation and an ability to model its occurrence.

There are two main phenomena that lead to hot tearing: (i) a lack of liquid feeding at high fraction of solid, ( $g_s$ ), and (ii) tensile or shear deformation transmitted through the partially coherent mushy zone.<sup>[1-7]</sup> The formation of hot tears is similar to porosity formation in the sense that it is linked to a lack of liquid feeding in the mushy zone, but requires additionally shear or tensile deformation in order to separate, or pull apart the solid network. These deformations occur due to the thermal gradients, solidification shrinkage, solid contraction and mechanical constraints, while the distribution and amount of intergranular fluid control the feeding of localized regions within the mushy zone.

Since grain morphology and size are characterized by a length scale much smaller than the process dimension, it is not surprising that most prior researchers have focused on macro

scale averaging methods for modeling the interaction between a deforming solid skeleton and intergranular fluid movement (e.g. [8-11]). In these works, a Representative Volume Element (RVE) is assumed to contain a mixture of solid and liquid, with local volume fractions  $g_s$  and  $g_l$ , respectively, interacting through the averaged conservation equations.<sup>[12]</sup> Unfortunately, such approaches are unable to describe any strain inhomogeneity at the grain level, in particular at grain boundaries where hot tears form. Furthermore, crack initiation and propagation involve the creation of local discontinuities, which are difficult to consider when using an averaging approach.

In order to account for this granular nature of semi-solids and strain inhomogeneity at the grain level, a number of so-called granular solidification models have been developed. Early models of this type considered a regular arrangement of grains that describe the ductility of the two-phase semi-solid [13] and liquid feeding [14]. However, such regular arrangements of grains do not approximate the microstructure very well, since all the solid grains percolate at the same time, *i.e.*, when  $g_s$  reaches unity. Recently, Vernède *et al.* [15] developed a 2D solidification model proposed originally by Mathier *et al.* [16], which does not have this shortcoming. In this model, grains are approximated by polyhedra based on the Voronoi diagram of a random set of nuclei, resulting in irregular grain arrangements. It has been shown that solidification predictions of this model are close to those of more refined approaches such as the pseudo-front tracking, but at a much lower computational cost [15]. The model is therefore ideally suited for granular simulations linking the behavior of a microscopic model to macroscopic properties of the material. Vernède *et al.* [17-18] have used this 2D granular approach to simulate the fluid flow caused by grain movement and solidification shrinkage in an Al-Cu alloy. Phillion *et al.* [19-20], using a similar approach based on 2D granular geometry, predicted the mechanical behavior of an equiaxed-granular semi-solid Al-Mg alloy.

In spite of the novelty introduced by the above granular models, it is clear that the behavior of the mushy zone cannot be modeled properly using 2D approaches since both semi-solid deformation and fluid flow through a granular domain are inherently 3D problems. For example, although simultaneous continuity of both the solid and liquid phases can exist in 3D, a topological feature of the 2D geometry is that for a given  $g_s$  only one of the two phases can be percolated through the domain.

In the present study, a 3D granular model based on the Discrete Element Method (DEM) has been developed in order to predict the stress-strain behavior of a collection of equiaxed-granular grains in the semi-solid state at a given  $g_s$ . DEM is a numerical method for computing the motion and deformation of a large number of particles. It was proposed in 1970s by Cundall and Strack [21] for rock mechanics problems, where the continuity between the entities does not exist. It has proved to be very useful for enhancing the understanding of granular and discontinuous materials in food science [22-23] and mining applications [21, 24]. Moreover, DEM is becoming widely accepted as an effective method for explaining experimentally observed facts in multiphase media [25-30]. At present, DEM has evolved from various disciplines including geomechanics, particle physics, and structural engineering.

The model presented in this work has been developed for a binary Al-2wt.%Cu alloy, due to its long freezing range, propensity for hot tear formation, and availability of experimental semi-solid constitutive data (e.g. [8, 10]). The mechanical behavior of the solid grains is modeled using a simple viscoplastic law, while the intergranular liquid has been replaced by connector elements. First, the methodology for generating the granular grain structure based on a solidification model is briefly described [31]. Second, a description of the semi-solid deformation model is provided with particular attention given to the link between the output of the solidification model and the input necessary for the mechanical calculation. The simulations are carried out using the FE software Abaqus 6.8 [32]. Third, the deformation

results from the FE/DEM simulation are discussed and validated against experimental data from the literature [8, 10].

## 2. Model development

### 2.1. Generation of Discrete Elements using a solidification model

The geometry for a FE/DEM simulation of semi-solid deformation is assumed to consist of equiaxed-granular solid grains surrounded by liquid films or channels. The grains are meshed as solid elements, while the liquid channels are not meshed, but are replaced by connector elements. Generation of this geometry requires a methodology for simulating the solidification of a large number of grains. Previous work by the authors [15-19, 33] has resulted in the development of a 3D granular solidification model known as GMS-3D [31], which is able to generate the required solid-liquid two-phase geometry at a fixed  $g_s$ . In this model, the grain structure is derived from a Voronoi tessellation of random nucleation centers. After construction of a 3D Voronoi diagram, shown in Figure 1(a), each Voronoi region, or grain (Figure 1(b)), is subdivided into polyhedral volume elements having the nucleation center as the summit and the Voronoi facet as the base (Figure 1(c)). These pyramids are further divided into tetrahedral elements in order to model solidification, by subdividing each Voronoi facet into triangles (Figure 1(d)). As in the previous model designed for 2D geometries [15-18] the solute exchange between tetrahedral pyramids is neglected in order to reduce the microsegregation model to a 1D problem in spherical coordinates. Microsegregation is assumed to be very fast in the liquid (perfect solute mixing) but with some back-diffusion in the solid. Thus, while all tetrahedral elements within a small pyramid solidify at the same speed, since they have the same perpendicular length  $L$  and hence the same Fourier number in the 1D solidification simulation, elements from different pyramids solidify at different rates, *i.e.*, different Fourier numbers. It should also be noted that, the facets of the polyhedral volume elements are not exactly continuous at edges. Such

approximations are necessary in order to speed up the computation to predict solidification and percolation of a large number of grains.

As in the previous 2D solidification model [15-18], the master diffusion equation controlling the evolution of the solid-liquid interface in a tetrahedron can be derived from a solute balance integrated over the solid and liquid phases. This equation is given below [31];

$$v^* x^{*2} (k_o - 1)C_l + \frac{1}{3}(L^3 - x^{*3}) \frac{\dot{T}}{m_l} + x^{*2} D_s \left. \frac{\partial C_s}{\partial x} \right|_{x^*} = 0 \quad (1)$$

where  $C_s$  and  $C_l$  are the solid and liquid composition,  $v^*$  is the velocity of the interface,  $x^*$  its actual position,  $k_o$  is the partition coefficient,  $D_s$  is the diffusion coefficient in the solid,  $\dot{T}$  is the cooling rate and  $m_l$  is the slope of the liquidus line. The evolution of the term  $\left. \frac{\partial C_s}{\partial x} \right|_{x^*}$  is determined by solving the diffusion equation in the solid phase using a finite difference scheme, a Landau transformation to follow the interface [34], and the boundary conditions:

$$\left. \frac{\partial C_s}{\partial x} \right|_{x=0} = 0 \quad \text{and} \quad C_s \Big|_{x=x^*} = C_s^* = k_o C_l.$$

At the beginning of the solidification, the liquid channels are very wide while near the end they are very narrow. Since small elements result in convergence issues during FE analysis, coalescence between two grains is assumed to occur when the thickness of the liquid channel between two elements is less than 0.4% of the average diameter of the grains. Although this hypothesis is not physically accurate, since the presence of very thin liquid films of a few nanometres in size have previously been observed near the end of solidification [35], these small films are highly viscous and tend also to stick two surfaces together. Thus, for hot tearing, very thin liquid channels act in a way similar to solid-solid bonds.

As  $g_s$  increases, and the width of liquid channels is reduced, coalescence of two neighbor grains occurs (typically once  $g_s > 0.9$ ) [36]. This creates clusters of increasing size, which ultimately percolate throughout the domain, *i.e.*, spread over the entire domain width. In

Section 3, it will be shown that the percolated solid at high  $g_s$  controls the mechanical resistance of the mushy zone.

## *2.2 FEM mechanical calculation*

The output of the solidification calculation at a given value of  $g_s$  is a set of solid tetrahedral elements, each one being in solid contact with three other solid elements belonging to the same grain. The fourth face is either in solid contact with the symmetric element of the neighbor grain or is separated from it by a liquid channel if coalescence has not yet occurred at that location (Figure 1). This output is then translated into a finite element mesh using a C++ subroutine within GMS-3D, which also automatically creates the Abaqus control file. As shown in Figure 2, four types of elements are involved in the finite element mesh of this geometry: (i) solid elements for the grains, (ii) multi point constraint (MPC) elements for the continuity between the facets of the same grain, (iii) contact elements, and (iv) flexible connector elements for the connectivity at grain boundaries. These last elements replace the liquid channels and are fitted to experimental data as explained in more details below.

In the present simulations of semi-solid deformation, the distribution of strain between the grains and in the intergranular region is of interest, while the detailed strain inhomogeneity within each grain is less relevant. Therefore, a coarse mesh for each grain has been used in order to be able to simulate a 3D RVE that contains a large number of grains.

### (i) Solid elements

Each solid tetrahedral element from the solidification calculation is split into two solid elements, a tetrahedron and a pentahedron, as shown in Figure 2(c). This split is made on a plane parallel to the solid-liquid interface, or grain boundary. As a result, there are approximately 100 solid elements per grain for the FEM mechanical calculation. The mechanical behavior of these solid elements is assumed to be elasto-viscoplastic. For the

simulations at low  $g_s$  (*i.e.*  $g_s < 0.94$ ), no solid bridges have formed between the grains [36-37] and the mechanical behavior of the free solid grains is relatively unimportant. This is because most of the deformation is concentrated in the liquid films and the stresses in the solid rarely exceed the yield stress. On the other hand, for simulations at high  $g_s$ , the mechanical behavior of a domain containing a large number of grain clusters is increasingly dictated by the behavior of the percolated grains. Physically, the mechanical behavior of each individual solid grain is anisotropic due to orientation dynamics (glide and climb) along preferred planes. Although such behavior is taken into account in detailed forming process models of solid materials [38-40], an idealized isotropic and elasto-viscoplastic model is considered for the solid phase owing to the high number of randomly oriented grains in each cluster of the RVE. This simplified constitutive description has been previously used for examining the mechanical behavior of Al-Cu alloys.[5, 8, 41-42] The isotropic elastic modulus,  $E=10$  GPa, and isotropic Poisson coefficient,  $\nu_{solid}=0.30$ , are taken from Ref. [8]. Since no hardening is observed in the experimental results of Al-Cu alloy at high temperature [41-42], once the stress reaches the elastic limit, the flow stress behavior of each grain is assumed to be perfectly plastic and based on a Norton-Hoff law:

$$\sigma(\dot{\epsilon}) = k \cdot \dot{\epsilon}^m \quad (2)$$

where  $\sigma$  is the stress,  $\dot{\epsilon}$  is the strain rate,  $k$  is a flow stress coefficient and  $m$  is the strain rate sensitivity coefficient of the material. Since the model is applied only over the range  $0.9 < g_s < 1$ , and the  $m$  and  $k$  do not change significantly over the corresponding range of temperature [41], constant values of  $m$  and  $k$  have been used. The values of  $k=54.4$  MPa.s and  $m=0.195$  are taken from Ref. [41]. Please note that when  $g_s = 1$ , equation (2) must predict the mechanical behavior measured in a fully solid specimen.

#### (ii) Multi point constraint (MPC) elements

As explained above, each tetrahedron shown in Figure 2 solidifies independently from its neighbors within any given grain without exchanging solute. Thus, the continuity between the facets of each grain is not conserved along solid liquid interface. In order to conserve continuity within a grain, MPC elements are used to tie the facets of each grain to its own neighbors. The MPC element joining two nodes provides a universal connection between their degrees of freedom, ensuring that the displacement of one node is identical to that of its neighbor.

### (iii) Contact elements

In order to prevent penetration between grains, contact elements are placed at the solid-liquid boundary of each grain. For this contact surface, a frictionless hard contact pressure – overclosure relationship is used. Thus, when surfaces are in contact, the pressure resulting from this interaction is transmitted, while the surfaces separate if the contact pressure reaches a value of zero. Computational cost is decreased using a finite-sliding, surface-to-surface contact formulation [32]. In Abaqus, this formulation uses a path-based tracking algorithm that carefully considers the relative paths of points on the slave surface with respect to the master surface, within each increment, in order to determine the contact zone<sup>[32]</sup>.

### (iv) Flexible connector elements

The connectivity between two neighbor grains prior to coalescence is modeled using connector elements. As shown in Figure 2, each connector consists of one link-spring element and one axial damper element that act in parallel to approximate the effects of the intergranular liquid phase. The link-spring simulates the effect of the hydrostatic pressure within the liquid, and thus controls the tensile forces required to separate two grains in a direction normal to the grain facets. This is because only the normal displacement leads to a

volume change within the liquid and consequently to a change in hydrostatic pressure. The damper operates on the relative velocities of the grains, acting as a dashpot between the grains, which simulates the viscosity effects of the intergranular liquid and thus controls the shear forces between two grains.

The result of the link-spring and the axial damper replacing the liquid is a surface force vector between grains that contains three components: a normal component ( $t_n$ ) and two shear tractions ( $t_s, t_e$ ). The nominal strain can thus be defined as;

$$\varepsilon_n = \frac{u_n}{l_o}, \quad \varepsilon_s = \frac{u_s}{l_o}, \quad \varepsilon_e = \frac{u_e}{l_o} \quad (3)$$

where  $u_n, u_s,$  and  $u_e,$  are the 3 corresponding displacement components and  $l_o$  is the original thickness of the liquid channel between the two grains. Furthermore, the corresponding force exerted by the spring-damper connector can be written as;

$$\begin{pmatrix} t_n \\ t_s \\ t_e \end{pmatrix} = \begin{pmatrix} K & 0 & 0 \\ 0 & 0 & 0 \\ 0 & 0 & 0 \end{pmatrix} \begin{pmatrix} \varepsilon_n \\ \varepsilon_s \\ \varepsilon_e \end{pmatrix} + \frac{C}{A} \begin{pmatrix} n \\ s \\ e \end{pmatrix} \dot{l} \quad (4)$$

where  $(n, s, e)$  are the components of the unit vector along the damper,  $\dot{l}$  the increasing rate of the length of the damper,  $A$  the area of the facet covered by each damper,  $K$  the elastic modulus of the spring and  $C$  the damping coefficient of the damper. The damping coefficient can be thought of as a force per relative velocity. There are several types of elements available in Abaqus that allow the user to define a flexible joint. In this simulation, the cohesive element COH3D6 with nil shear modulus has been used for the spring and the CONN3D2 element has been used for the damper.

At present, constant values of  $C$  and  $K$  have been used, as the model is applied only over the range  $0.9 < g_s < 1$ , which corresponds to the vulnerable range for hot tears formation and thus the interesting range for hot tearing simulations. The values of  $C$  and  $K$  were

determined as follows. First, stress-strain curves obtained from series of tensile deformation simulations were generated for a given  $g_s$ , strain rate and different values of  $C$  and  $K$ . Second, these stress-strain curves were compared to semi-solid tensile test experimental results [8]. The values of  $C$  and  $K$  giving the best fit were determined and then used for all the other simulation results. More details on this fitting procedure are provided in Section 3. Although constant values of  $C$  and  $K$  have been used for the present work, it is clear that the liquid film resistance to separation and shear actually depends on its ability to be fed, and thus on its location within the domain, as shown in 2D by Vernède et al. [17]. This type of feeding calculation is currently being developed and will be iteratively coupled, in a future work, to the present model, so that the  $C$  and  $K$  values of each flexible connector can be varied during the simulation

### 2.3 Domain Size and Boundary Conditions

As shown in Ref. [43], the FE / DEM granular model requires a domain containing a minimum of 700 grains in order to accurately model semi-solid deformation. Above this number, the behavior of the domain does not depend on the number and/or distribution of grains, *i.e.*, the domain can be considered as a RVE of the mushy zone. In the simulations described below, the number of grains within the RVE is 864, with an average grain size of 100  $\mu\text{m}$ . Symmetry boundary conditions are imposed on the surfaces  $x=0$ ,  $y=0$  and  $z=0$ , while the surfaces  $y=L_y$  and  $z=L_z$  are free to move and the surface  $x=L_x$  is connected to a reference node. The variables  $L_x$ ,  $L_y$ , and  $L_z$  refer to the length of the RVE along the  $x$ ,  $y$ , and  $z$  directions respectively. To deform the RVE, an imposed displacement is applied to the reference node linked to the surface  $x=L_x$ , *i.e.*, a Dirichlet condition with fixed displacement is imposed on this boundary. The use of a reference node enables the bulk semi-solid mechanical behavior to be obtained directly from the calculated force–displacement curve at this location.

### 3. Results and discussion

#### 3.1 Determination of $C$ and $K$

The damping coefficient  $C$  and spring constant  $K$  for the flexible connectors are determined via a fitting exercise and comparison to experimental data obtained for an Al-2wt.%Cu semi-solid specimen [8]. First, it must be noted that in order to deform the RVE at a uniform strain rate  $\dot{\epsilon}$ , the velocity of the reference point is abruptly increased from zero to a uniform velocity given by  $(\dot{\epsilon} \times L_x)$ . Since the bulk stress of a semi-solid material due to its viscosity (average “viscosity” of the solid and liquid) is a function of the velocity, the initial simulated stress-strain behavior presents a sharp stress increase. A similar initial stress increase is also actually observed in experimentally-measured semi-solid tensile stress-strain curves [8, 44]. According to this initial increase, the damping coefficient  $C$  can be estimated, while  $K$  can be estimated from the slope of the stress-strain curve after this initial transient.

The fitting exercise is shown in Figure 3, in which the simulated bulk stress-strain curves obtained at  $g_s = 0.94$  and  $\dot{\epsilon} = 0.001 \text{ s}^{-1}$  for various values of (a)  $K$  and (b)  $C$  are compared to tensile test experimental results at the same  $g_s$  [8]. In this figure, the experimental curve is shown as a solid line, while the simulated curves are shown as dashed lines with symbols. As can be seen by comparing the curves of (a) and (b), the initial stress increase is a function of  $C$  but not of  $K$ . However, the slope of these curves after the primary increase depends only on  $K$ , but not on  $C$ . Using this series of simulations, a value of  $C = 2 \times 10^3 \text{ N.s/m}$  for the damping coefficient, and a value of  $K = 2.3 \text{ MPa}$  for the elastic modulus of the spring were chosen. These values will be used in all the simulation results presented here after. Note also that, since there is no failure model included in the numerical computations, the stress-strain curves do not exhibit the maximum seen in the experimental data.

### 3.2 Tensile deformation

In Figure 4, a comparison is made between the simulated stress-strain predictions and the experimental results for the same Al-2wt.%Cu alloy from [8], over a range of fractions of solid between 0.92 and 0.98 at a strain rate of  $\dot{\epsilon} = 0.001 \text{ s}^{-1}$ . Beginning with the experimental data, it can be seen that for all tests, the stress increases with increasing strain as expected and reaches a maximum value  $\sigma_{\max}$ , before failure occurs. However, two different types of behavior are observed. For  $g_s = 0.92, 0.94, \text{ and } 0.96$ , the stress gradually increases until it reaches the maximum value  $\sigma_{\max}$ , whereas at  $g_s = 0.98$ , the stress increase is larger because more grains have percolated, thus increasing the stiffness of the semi-solid material. Some hardening is also visible in all four curves. During the initial stages of deformation, the role of the percolated solid is dominant but once the percolated solid yields, the behavior is mainly dictated by the contact and deformation of the free grains. Hence, although the behavior of the solid grains is actually elastic – perfectly plastic, the behavior of the entire semi-solid material is not, as can be seen in Figure 4, but instead undergoes geometric strain hardening [19] during deformation. An initial stress increase can also be observed in the results for  $g_s=0.94$  and  $g_s=0.98$ . In the same figure, the results of the FE/DEM model are also presented. As can be seen, they reproduce correctly the general trends of the experimental curves for the four values of  $g_s$ ; the value  $g_s=0.94$  showing the best agreement since it was used in Figure 3 for the calibration of  $C$  and  $K$ .

To investigate the tensile mechanical behavior of the model at different strain rates, the simulated results are compared to experimental results of Ref. [10], which also used an Al-2wt%Cu alloy. As can be seen in Figure 5, the results of the model reproduce quite accurately the general trends of the experimental curves, obtained at  $0.001$  and  $0.004 \text{ s}^{-1}$  strain rates. The values for  $C$  and  $K$  were identical in both cases, and taken from Section 3.1. The results from two other simulations, using strain rates of  $10^{-4}$  and  $10^{-2} \text{ s}^{-1}$ , are also shown.

Although these results could have been produced using an averaging constitutive model, such as the one developed by Mathier *et al.* [10] containing an internal variable related to the evolution of coherency, such alternative approaches cannot give access to stress and strain inhomogeneities such as those to be shown in Figure 6 and Figure 7.

Figure 6 shows strain contours from cross sections within the RVE for three values of  $g_s$  ( $g_s=0.92$ ,  $0.96$ , and  $0.98$ ), outlined in Figure 4, when the overall or bulk strain is 1%. The deformation is horizontal and to the right. As can be seen, strain localization is concentrated within the liquid films located between the grains *i.e.*, is accommodated by the dampers and springs. For the two images at lower  $g_s$ , Figure 6(a) and Figure 6(b), the strain is fairly well distributed in the liquid channels perpendicular to the tension direction. However, when  $g_s=0.98$ , Figure 6(c), the strain appears to be localized along few preferential paths. Also, the maximum local strain for  $g_s=0.98$  is predicted to be about four times larger than the maximum local strain for  $g_s=0.92$ , and is two orders of magnitude larger than the bulk strain of the RVE.

Figure 7 shows the contour plots of the Von Mises stress in (MPa) for  $g_s=0.98$  at (a) the boundary surface and (b) a slice inside the RVE. In this figure, it can be seen that percolated grains transmit the load from the left to the right face of the RVE. In this case, solid bridges act as the main obstacles to the fracture of the semi-solid material in tension.

### 3.3 Compression deformation

It is well known that the tensile and compressive behavior of semi-solid materials is drastically different [8, 45-46]. In the mushy zone, compressive deformation is similar to the squeezing of a sponge, causing the intergranular liquid to flow out and the pressure within this liquid to increase. Figure 8 shows the simulated mechanical behavior of the mushy zone in compression as a function of  $g_s$  for the same parameters  $C$  and  $K$  used in tension. While at low strain the behavior of the semi-solid in tension and compression is similar, the

compressibility of the mush decreases and approaches the incompressibility of a fully solid structure ( $g_s=1$ ) as soon as the liquid between grains has been removed and the grains come into contact with each other. The start of incompressibility is defined as the inflection point in a stress-strain curve, *i.e.*,  $d^2\sigma/d\varepsilon^2=0$ , and is the point in the model when the contact elements activate at the grain boundaries. As can be seen by the large black circles in Figure 8, the start of incompressibility occurs at  $\varepsilon=0.003$  for  $g_s=0.98$ , but increases to  $\varepsilon=0.011$  and then  $\varepsilon=0.016$  when  $g_s$  decreases to 0.96 and 0.94, respectively, and more liquid is present between grains. However, please note that the maximum stress that can be modeled is limited due to contact convergence difficulties. As can be seen in Figure 8 the maximum stress decreases with decreasing  $g_s$ , because the number of clusters increases.

### 3.4 Shear deformation

Figure 9 shows the simulated mechanical behavior of the RVE under shear deformation and the experimental results of an Al-2wt.%Cu alloy being sheared in the semi-solid state between two coaxial cylinders [8]. The experimental test consists of imposing a constant velocity to the inner cylinder along the longitudinal axis while the experimental test specimen is held at a given temperature. As the spacing between the two cylinders remains constant, this test did not correspond to a simple shear, but rather to an in-plane shear with a small tensile component along the cylinder radius. Although this component is small at low strain, it becomes important and leads to higher values of the Von Mises stress with increasing strain.

As can be seen in Figure 9, the agreement between the simulated shear deformation curves and the experimental results is satisfactory for low strain and low  $g_s$  ( $g_s=0.92$ , *i.e.* prior to the formation of solid bridges). At higher strain, however, the calculated stress for  $g_s=0.92$  is below the experimental curve. This result can probably be attributed to the difference between the simulated simple shear and the experimental in-plane shear. At high  $g_s$

( $g_s=0.98$ ), the model also reproduces correctly the initial behavior of the mushy zone but then over predicts the stress beyond approximately  $\varepsilon=0.3$ . This deviation could be linked to the rupture of the connections (bridges) between percolated grains. While thin films of liquid do not allow two grains to be pulled apart in tension without liquid feeding, these films allow grains to slip across each other since no volume change is involved. As mentioned, this model assumes the very thin liquid channels to act in a way similar to solid-solid bonds. In order to reproduce the experimentally observed behavior of the mushy zone at high  $g_s$  under shear deformation, a failure criterion of the solid-solid bonds in shear would need to be added to the model. On the other hand, the no-slip condition experimentally assumed to exist at the cylinder surface might not be respected at high strain rate.

### *3.5 Comparison of the 3 Deformation Modes*

The simulation results presented for tension, compression and shear show that the model is able to predict different behavior for the different mechanical tests. Figure 10 shows a comparison of the behavior of the mushy zone under these three deformation modes. As can be seen, the deformability, i.e. the amount of strain for a given stress, is lower in compression as compared to tension since the intergranular liquid can flow out to allow for solid contact between grains. The inflection point and/or the beginning of incompressibility, is the starting point of the deviation of the compressive curve from the tensile curve. Below this point, the mechanical behavior of mushy zone is controlled by the deformation of the percolated grains and the connector elements, and thus is the same. However above the inflection point, the mechanical behavior in compression is affected by the solid contacts between the grains whereas in tension the behavior remains controlled only by the deformation of the percolated grains and the connector elements.

Under shear deformation, the normal link-spring behaves in a similar fashion to intergranular liquid and allows the solid grains to slip over on each other lower. In this case,

the semi-solid deformability is higher as compared to tensile behavior. Experimental results for aluminum alloys also demonstrate this variability and show different semi-solid tension, compression and shear mechanical behavior.

#### **4. Conclusion**

A 3D granular model has been developed based on the Discrete Element Method in order to predict the mechanical behavior of semi-solid metallic alloys. The initial geometry of the semi-solid at a given volume fraction of solid was obtained from a 3D granular model of solidification [31]. The elements making up the solid grains were modeled using elasto-viscoplastic behavior, along with contact surfaces to limit inter-grain penetration. The grain-interactions prior to complete solidification, *i.e.* the behavior of the intergranular liquid, were simulated through the use of connector elements. Each connector consisted of one link-spring element and one damper element acting in parallel to approximate the hydrostatic and shear behavior of the liquid. The model predictions have been validated successfully against prior literature experimental results [8, 10], using only two fixed parameters. Both parameters  $C$  and  $K$  were held constant over the range of  $g_s$  investigated.

In comparison to averaging methods using internal variables and/or complex behavior, the combined FE / DEM is able to predict the inhomogeneous strain distribution in a semi-solid RVE. This technique can be used because the interest with respect to hot tearing and other solidification defects lies in understanding the mechanical behavior of a collection of grains, with a random distribution of nucleation centers, while the detailed deformation within a single grain, and/or the fluid velocity within a single channel can be approximated. The limitations of this model are as follows:

(1) The model can predict the behavior of mushy zone only in the range of  $g_s$  between 0.9 and 1. For  $g_s$  lower than 0.9, the mechanical properties of the solid grains, and the values used for  $C$  and  $K$  must be re-evaluated.

(2) The model can predict the behavior of the mushy zone only under small deformations and limited strain rate.

(3) The model cannot predict the behavior of the mushy zone after damage initiation since such prediction requires the consideration of the intergranular liquid flow, induced by solidification shrinkage and by the opening of wet grain boundaries. This limitation is the subject of current research by the authors, in order to localize the pressure drop in the remaining liquid and to propose a defect nucleation criterion.

## 5. Acknowledgements

The authors would like to thank the Swiss Competence Centre for Materials Science and Technology (CCMX), and partner companies within the thematic area “Multi-scale, multi-phenomena modelling of metallic systems” for funding this research.

## 6. References

1. J. Campbell, *Materials Science and Technology*, 1991, vol. 7, pp. 885-94.
2. T. W. Clyne, G. J. Davies, *British Foundrymen*, 1975, vol. 68, pp. 238-44.
3. T. W. Clyne, M. Wolf, W. Kurz, *Metall. Trans. B*, 1982, vol. 13B, pp. 259-66.
4. J. A. Danzing, M. Rappaz, *Solidification*. Editor, EPFL Press, Lausanne, 2009.
5. J. M. Drezet, O. Ludwig, M. M'Hamdi, H. G. Fjaer, C. L. Martin, *Light metals, The Minerals Metals and Materials Society, USA, TMS, Warrendale, PA, 2004*, pp. 655-60.
6. C. A. Monroe, C. Beckermann, J. Klinkhammer, *Modeling of Casting, Welding, and Advanced Solidification Processes - Xii*, S. L. Cockcroft, D. M. Maijer, eds., 2009.
7. M. Rappaz, J. M. Drezet, M. Gremaud, *Metall. Trans. A*, 1999, vol. 30, pp. 449-55.
8. O. Ludwig, J. M. Drezet, C. Martin, M. Suéry, *Metall. Trans. A*, 2005, vol. 36, pp. 1525-35.
9. V. Mathier, J. M. Drezet, M. Rappaz, *Modell Simul Mater Sci Eng*, 2007, vol. 15, pp. 121-34.
10. V. Mathier, S. Vernède, P. Jarry, M. Rappaz, *Metall. Trans. A*, 2009, vol. 40, pp. 943-57.
11. M. M'Hamdi, A. Mo, C. L. Martin, *Metall. Trans. A*, 2002, vol. 33, pp. 2081-93.
12. J. Ni, C. Beckermann, *Metall. Trans. B*, 1991, vol. 22, pp. 349-61.
13. D. J. Lahaie, M. Bouchard, *Metall. Trans. B*, 2001, vol. 32, pp. 697-705.
14. W. O. Dijkstra, C. Vuik, A. J. Dammers, L. Katgerman, *Solid Proc & Microst: Symp Hon of W Kurz*, M. Rappaz, C. Beckerman, R. Trivedi, eds., TMS, 2004, pp. 151-56.
15. S. Vernède, M. Rappaz, *Acta Materialia*, 2007, vol. 55, pp. 1703-10.
16. V. Mathier, A. Jacot, M. Rappaz, *Mod Sim Mater Sci Eng*, 2004, vol. 12, pp. 479-90.
17. S. Vernède, J. A. Dantzig, M. Rappaz, *Acta Materialia*, 2009, vol. 57, pp. 1554-69.

18. S. Vernède, P. Jarry, M. Rappaz, *Acta Materialia*, 2006, vol. 54, pp. 4023-34.
19. A. B. Phillion, S. L. Cockcroft, P. D. Lee, *Acta Materialia*, 2008, vol. 56, pp. 4328-38.
20. A. B. Phillion, S. L. Cockcroft, P. D. Lee, *Modelling and Simulation in Materials Science and Engineering*, 2009, vol. 17, pp.
21. P. A. Cundall, O. D. L. Strack, *Geotechnique*, 1979, vol. 29, pp. 47-65.
22. Y. J. Sun, W. L. Xu, *15th International Conference on Mechatronics and Machine Vision in Practice (M2vip)*, Auckland, New Zealand, 2008, pp. 201-07.
23. K. M. Wright, J. Sprunt, A. C. Smith, B. P. Hills, *International Journal of Food Science and Technology*, 2003, vol. 38, pp. 351-60.
24. P. A. Cundall, *Proceedings of the Institution of Civil Engineers-Geotechnical Engineering*, 2001, vol. 149, pp. 41-47.
25. M. A. Delele, E. Tijssens, Y. T. Atalay, Q. T. Ho, H. Ramon, B. M. Nicolai, P. Verboven, *Journal of Food Engineering*, 2008, vol. 89, pp. 33-41.
26. G. Frenning, *Computer Methods in Applied Mechanics and Engineering*, 2008, vol. 197, pp. 4266-72.
27. K. Han, D. Peric, A. J. L. Crook, D. R. J. Owen, *Engineering Computations*, 2000, vol. 17, pp. 593-619.
28. A. Munjiza, K. R. F. Andrews, *Int. J. Num. Meth. Eng.*, 2000, vol. 49, pp. 1377-96.
29. H. Peron, J. Y. Delenne, L. Laloui, M. S. El Youssoufi, *Computers and Geotechnics*, 2009, vol. 36, pp. 61-69.
30. T. G. Sitharam, *Current science*, 2000, vol. 78, pp. 876-86.
31. A. B. Phillion, J. L. Desbiolles, M. Rappaz, *Modeling of Casting, Welding, and Advanced Solidification Processes - Xii*, Vancouver, Canada, S. Cockcroft, D. Maijer, eds., TMS, Warrendale, PA, 2009, pp. 353-60.
32. Abaqus, *Abaqus Theory Manual Version 6.8-2*, RI 02909-2499, USA, 2008.
33. A. B. Phillion, S. Vernede, M. Rappaz, S. L. Cockcroft, P. D. Lee, *Int. J. Cast Met. Res.*, 2009, vol. 22, pp. 240-43.
34. V. R. Voller, S. Sundarraj, *material science technology*, 1993, vol. 9, pp. 474-81.
35. I. Farup, J. M. Drezet, M. Rappaz, *Acta Materialia*, 2001, vol. 49, pp. 1261-69.
36. M. Rappaz, A. Jacot, W. J. Boettinger, *Metall. Trans. A*, 2003, vol. 34, pp. 467-79.
37. M. Rappaz, J. M. Drezet, P. D. Grasso, A. Jacot, *Modeling of Casting, Welding and Advanced Solidification Processes-X*, Stefanescu, Warren, Jolly, Krane, eds., TMS, Warrendale, PA, 2003, pp. 53-60.
38. P. Van Houtte, A. Van Bael, S. He, *Materials Processing and Design: Modeling, Simulation and Applications*, Pts I and II, J. M. A. César de Sá, A. D. Santos, eds., 2007, pp. 159-64.
39. P. Van Houtte, A. Van Bael, M. Seefeldt, *5th international conference on processing & manufacturing of advanced materials*, Vancouver, Canada, 2006, pp. 3454-59.
40. P. Van Houtte, A. Van Bael, M. Seefeldt, *Fundamentals of Deformation and Annealing*, 2007, vol. 550, pp. 13-22.
41. B. Magnin, L. Maenner, L. Katgerman, S. Engler, *Mater. Sci. Forum*, 1996, vol. 217-222, pp. 1209-14.

42. P. Wisniewski, H. D. Brody, *Modeling of Casting, Welding, and Advanced Solidification Processes V*, M. Rappaz, M. R. Ozgu, K. W. Mahin, eds., TMS, Warrendale, PA, 1991, pp. 273-78.
43. M. Sistaninia, A. B. Phillion, J. M. Drezet, M. Rappaz, *49th Annual Conference of Metallurgists, Vancouver, BC, 2010*.
44. S. Vernède, PhD. *PhD Thesis, EPFL, Lausanne, 2007*.
45. D. G. Eskin, Suyitno, L. Katgerman, *Prog. Mater. Sci.*, 2004, vol. 49, pp. 629-711.
46. W. M. van Haafden, W. H. Kool, L. Katgerman, *Mater. Sci. Eng. A*, 2002, vol. 336, pp. 1-6.

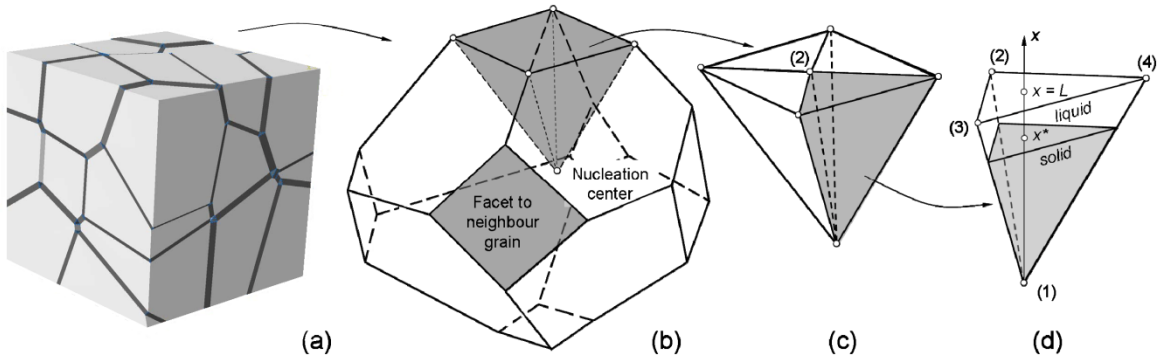


Figure 1 - A breakdown of the geometry describing the 3D granular solidification model (a) the entire model domain; (b) a polyhedral grain; (c) a pentahedral volume element; (d) a single tetrahedral element showing both the solid portion (grey) and liquid portion (clear)<sup>[31]</sup>

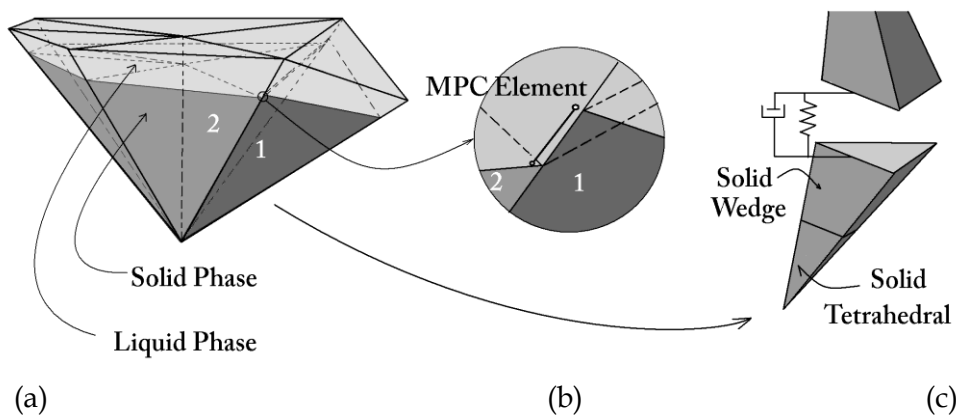
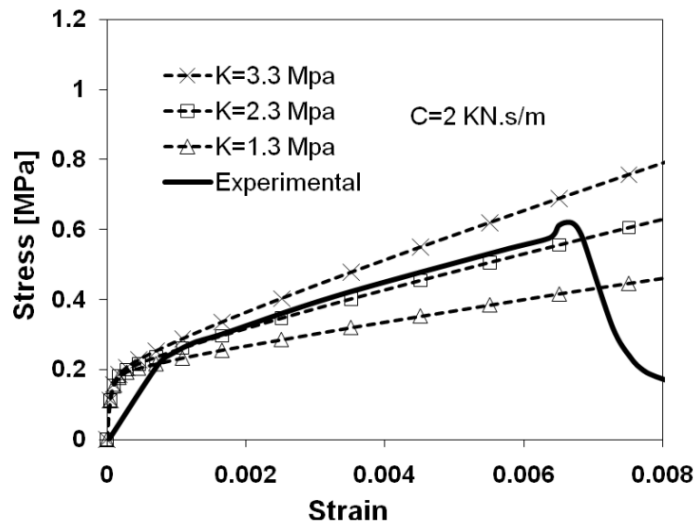
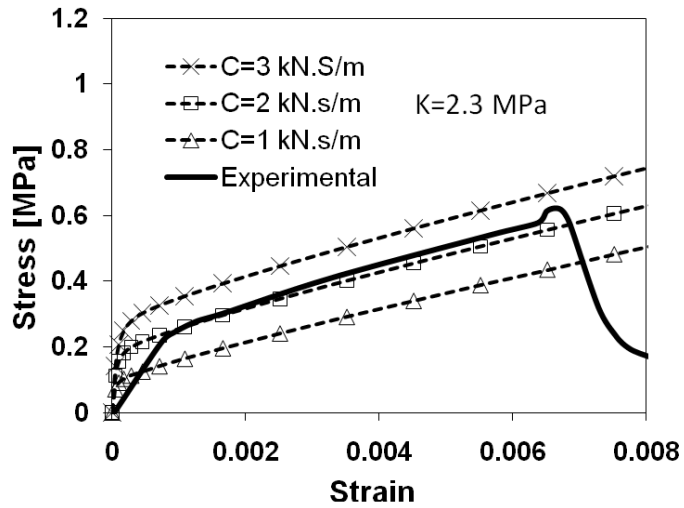


Figure 2 - The different elements involved in the FE model together with the connections between them, (a) one volume element (Figure 1(c) decomposed into a set of tetrahedrons (b) the MPC constraint between two nodes belonging to the same grain (c) a connector element between two nodes across a grain boundary



(a)



(b)

Figure 3-A comparison between tensile test experimental result for Al-2wt.%Cu [8] and the results of the model for  $g_s = 0.94$  and for each (a) spring moduli K and (b) damping coefficients C

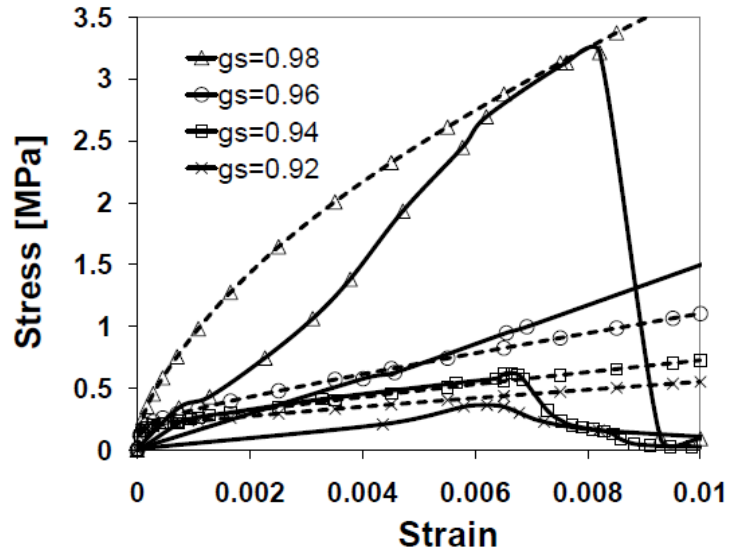


Figure 4-Tensile behavior of partially solidified Al-Cu alloys Al-2wt.%Cu: stress vs. strain curves from experimental data (continuous curves) [8] and from the model (dashed line curves) for various fraction of solid:  $\times$   $g_s = 0.92$  ( $T = 883$  K);  $\square$   $g_s = 0.94$ ;  $\circ$   $g_s = 0.96$  ( $T = 858$  K);  $\Delta$   $g_s = 0.98$  ( $T = 824$  K)

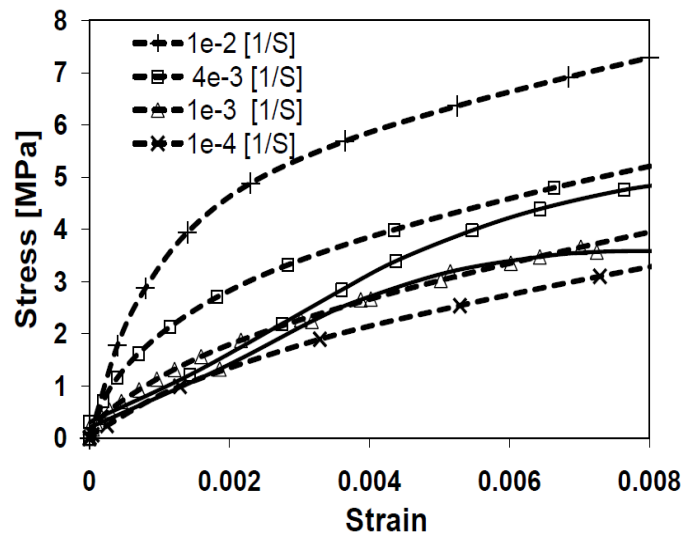


Figure 5-Comparison between the tensile experimental results of partially solidified Al-2wt.%Cu alloys [10] (continuous curves) and simulation results (dashed line curves) for  $g_s = 0.99$  ( $T = 813$  K) and different strain rates.

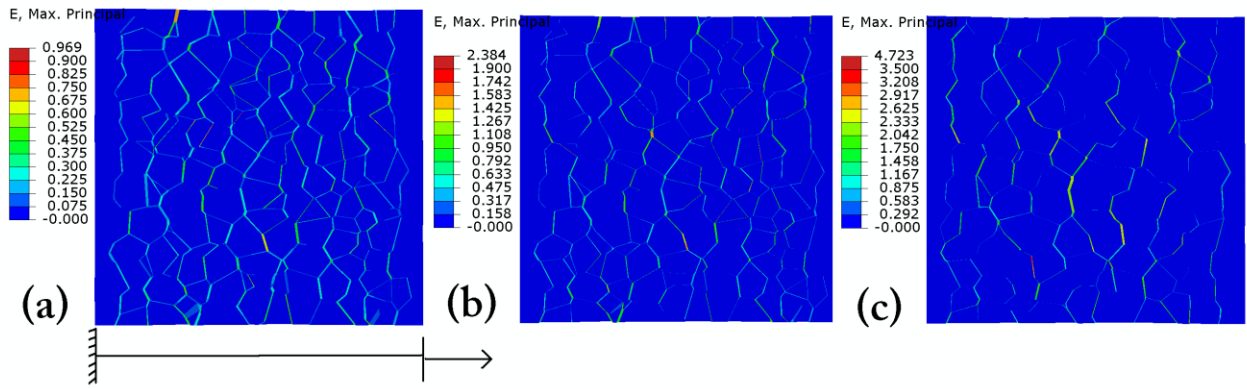


Figure 6-Finite-element simulation showing strain localization through an isothermal mushy zone volume element ( $1.2 \times 1.2 \times 6 \text{ mm}^3$ ) under tensile deformation for (a)  $g_s = 0.92$ ; (b)  $g_s = 0.96$ ; (c)  $g_s = 0.98$

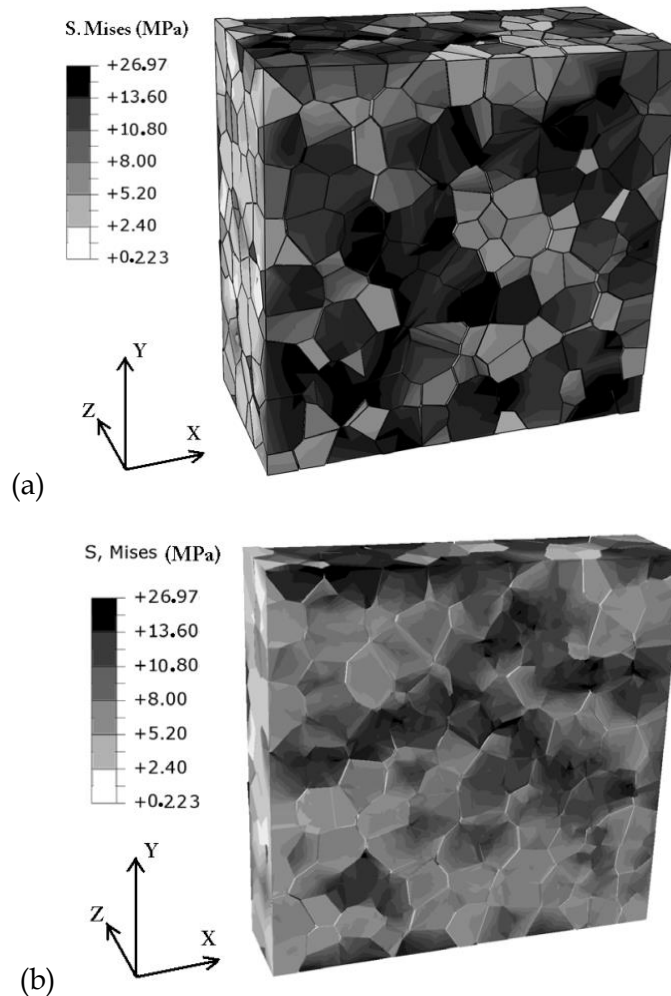


Figure 7-Contour plot of the Von Mises stress for tensile deformation of  $g_s = 0.98$  and corresponding value (MPa) on (a) outer surface (b) a cross section inside the domain

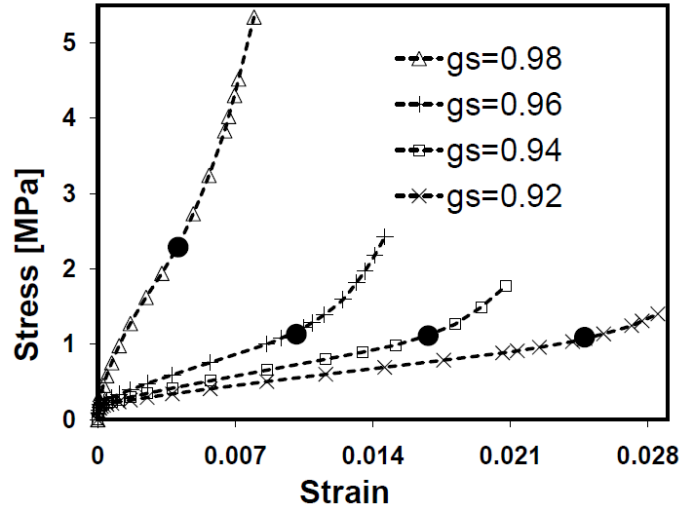


Figure 8-Compression behavior of Al- 2wt% Cu alloys: stress vs. strain curves from the model for various fraction of solid:  $\times g_s = 0.92$ ;  $\square g_s = 0.94$ ;  $+ g_s = 0.96$ ;  $\Delta g_s = 0.98$ . The large black circles represent the beginning of incompressibility.

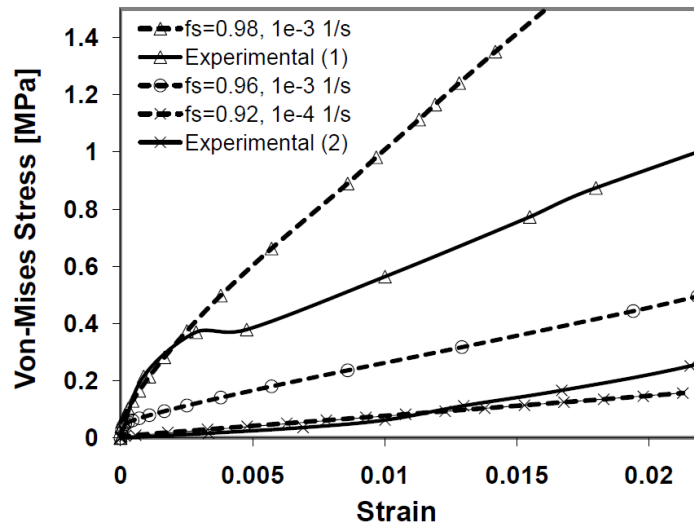


Figure 9-Shear behavior of Al- 2wt% Cu alloys: stress vs. strain curves from experimental data (continuous curves) (1)  $T=823\text{ K}$ ,  $\dot{\epsilon}=1e-3\text{ s}^{-1}$  and (2)  $T=883\text{ K}$ ,  $\dot{\epsilon}=1e-4\text{ s}^{-1}$  [8] and from the model (dashed line curves) for various fraction of solid:  $\times g_s = 0.92$ ;  $\circ g_s = 0.96$ ;  $\Delta g_s = 0.98$

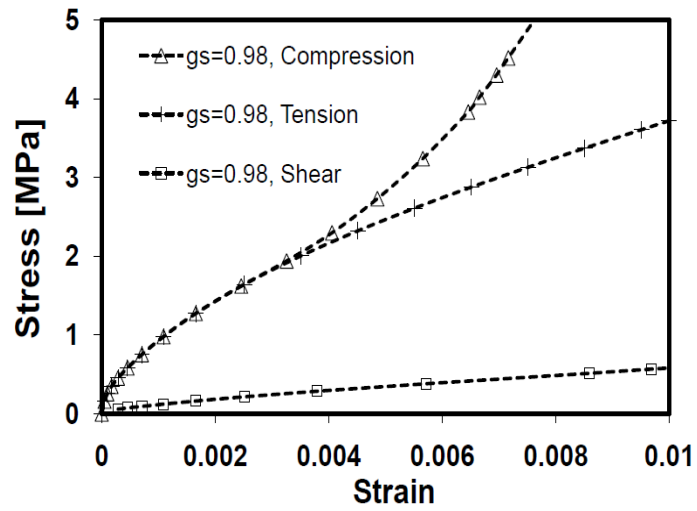


Figure 10 -A comparison of the behavior of the mushy zone under shear, compressive and tensile loading at  $g_s = 0.98$